A simplified model to evaluate peak amplitude for vertical vortex-induced vibration of bridge decks

Mingjie Zhang[a,b], Fuyou Xu[a,*], Haiyan Yu[a]

[a] *School of Civil Engineering, Dalian University of Technology, Dalian 116024, China*

[b] *Department of Structural Engineering, Norwegian University of Science and Technology, Trondheim 7491, Norway*

Abstract: A simplified model is developed to conveniently evaluate the peak vortex-induced vibration (VIV) amplitudes of a bridge deck at various mass-damping conditions. As a simplified form of the describing function-based model previously developed by the authors, the key innovation of the new model is the introduction of an envelope curve of the aerodynamic describing functions (or amplitude-dependent flutter derivatives), which determines the maximum negative aerodynamic damping versus vibration amplitude in the lock-in range. Based on the envelope curve, the peak VIV amplitudes at different mass-damping conditions can be obtained directly without calculating all the VIV amplitudes in the entire lock-in range. The new model is more practical for engineers in the bridge engineering community since it only contains a single group of aerodynamic parameters which don't vary with the reduced wind speed. The envelope curve can be either identified based on the VIV decay-to-resonance and/or grow-to-resonance signals at a single mass-damping condition, or based on the VIV steady amplitudes at different mass-damping conditions. Numerical examples involving the VIV analyses of a rigid rectangular cylinder and a bridge deck sectional model are utilized to validate the simulation accuracy of the proposed model, and the model is applied to calculate the peak VIV amplitudes of two flexible bridge decks at various mechanical damping levels. The proposed model is capable of accurately and conveniently predicting the peak VIV amplitudes of a bridge deck sectional model at various mass-damping conditions. For a flexible bridge deck, the peak VIV amplitude calculated by the proposed model is slightly conservative due to the overestimated negative aerodynamic damping at some span-wise segments of the bridge deck. The superiority of the proposed model relative to the conventional van der Pol-type model is also demonstrated.

Keywords: Vortex-induced vibration; Aerodynamic damping; Bridge deck; Mass-damping condition.

* Corresponding author.
E-mail addresses: mingjie.zhang@ntnu.no (M.J. Zhang); fuyouxu@hotmail.com (F.Y. Xu); haiyanyu92@hotmail.com (H.Y. Yu)

1. Introduction

Long-span, flexible bridges are vulnerable to vortex-induced vibrations (VIVs), which may seriously impact the structural fatigue life and/or the traffic safety. In the past two decades, VIVs with relatively large-amplitude limit cycle oscillations have been reported for a lot of operational bridges, e.g., the Trans-Tokyo Bay crossing Bridge [1], the Volgograd Bridge [2], the Jindo Bridge [3], the Xihoumen Bridge [4], and mostly recently, the Humen bridge [69]. The frequent occurrences of VIVs therefore call for great attentions to assess the VIV of a bridge in the preliminary design stage.

The most direct approach to evaluate the VIV performance of a design scheme is to conduct wind tunnel tests on a scaled full-bridge aeroelastic model with the same structural dynamic property and aerodynamic configuration as the prototype. However, full-bridge aeroelastic test is not only time consuming but also expensive in terms of the investment of large-size wind tunnel and the energy consumption. More importantly, due to the very small scaling ratio (e.g., 1/100 ~ 1/200) of the aeroelastic model, the experimental results may be unreliable as a result of the Reynolds number effect and other unsatisfied similarity rules (e.g., the aerodynamic configuration) [5-9]. On the other hand, wind tunnel tests can be conducted on a bridge deck sectional model with larger scaling ratio in order to obtain more accurate results with reduced experimental efforts [10-15]. To assess the VIV response of the full bridge, a mathematical model for the vortex-induced force is thereby required since the sectional model tests cannot consider the effects of mode shape, structural nonlinearity, and non-uniform flow condition, etc. The aerodynamic parameters of the mathematical model can be extracted based on the sectional model tests.

Extensive investigations on modeling the VIV of circular cylinders have led to several well-known semi-empirical mathematical models, among which the most famous ones are the wake-oscillator model [e.g., 16-22] and the force decomposition model [e.g., 23-28]. To simulate the VIV of bridge decks, Scanlan [29] suggested a van der Pol-type oscillator to model the vortex-induced forces acting on bridge decks. In Scanlan's model, the limit cycle oscillation of VIV is essentially due to the nonlinear aerodynamic damping with a prescribed expression. Following this suggestion, a number of studies have been carried out to enhance the model parameter identification procedure [30-32]. However, the parameters in Scanlan's model may vary irregularly and significantly with the mechanical damping ratio (and hence the dimensionless mass-damping parameter, i.e., Scruton number, *Sc*) of the bridge deck [30, 33, 67]. As a result, Scanlan's model may fail to predict the VIVs of a bridge deck at various *Sc* [33, 34]. To improve the predictive capability of the van der Pol-type model, several studies have been conducted to improve the nonlinear aerodynamic damping expression [35-39]. Other recent attempts to model the VIV of bridge decks can be found in [40-44]. Although the aforementioned models are more accurate than Scanlan's model in simulating the VIV of bridge decks, they are definitely more complicated in terms of both model expressions and parameter identifications. Furthermore, the applicability of these models in calculating the VIV of a real bridge in complex wind environment requires in-depth validation.

Indeed, the most important concern in practical VIV analysis of a bridge deck is to evaluate the peak amplitude, while the lock-in range can be roughly estimated according to its modal frequencies and Strouhal number. However, since the peak VIV amplitudes occur at different reduced wind speeds for various *Sc*, it is generally necessary to calculate all the VIV amplitudes in the entire lock-in range in order to determine the peak amplitudes of a bridge deck. To this end, a simplified model is developed in the present paper to more conveniently evaluate the peak VIV amplitudes of a bridge deck at various *Sc*. The new model is essentially a simplified form of the describing function-based model developed in [34]; the key innovation is the introduction of an envelope curve of the aerodynamic describing functions, by which the peak VIV amplitudes at various *Sc* can be conveniently evaluated without calculating all the VIV amplitudes in the entire lock-in range. The new model is more practical for engineers in the bridge engineering community since it only contains a single group of aerodynamic parameters which don't vary with the reduced wind speed.

The following part of the present paper is organized as follows: the governing equations for the VIVs of a spring-suspended bridge deck sectional model and a flexible bridge deck are presented in Section 2; details of the proposed VIV model are introduced in Section 3; Section 4 discusses the identification of aerodynamic parameters; numerical examples involving the VIV analyses of a rigid rectangular cylinder and a bridge deck sectional model are presented to validate the accuracy of the proposed model, and the model is utilized to calculate the peak VIV amplitudes of two flexible bridge decks at various mechanical damping levels in Section 5; finally, some conclusions are summarized in Section 6.

2. Governing equation for vertical VIV of a bridge deck

This paper focuses on the engineering modeling of the vertical VIV of a bridge deck in two-dimensional flow. A spring-suspended bridge deck sectional model immersed in two-dimensional flow is schematically shown in Fig. 1, in which m is the mass per unit span length, k_0 is the spring stiffness constant, c_0 is the mechanical damping coefficient, U is the mean wind speed, α_0 is the initial wind angle of attack; y is the vertical displacement; F is the vortex-induced force acting on the bridge deck per unit span length, which is to be modeled in this paper. The governing equation for the vertical VIV of the bridge deck sectional model can be expressed as

$$m(\ddot{y} + 2\xi_0\omega_0\dot{y} + \omega_0^2 y) = F(t) \tag{1}$$

where overdot represents the derivative with respect to time t; $\omega_0 = (k_0/m)^{0.5}$ is the natural circular frequency; $\xi_0 = c_0/(2m\omega_0)$ is the mechanical damping ratio.

Field measurements on full-scale bridges and wind tunnel tests on aeroelastic models suggest that the VIV of a flexible bridge is dominated by a single mode. Accordingly, the VIV analysis of a flexible bridge can be simplified as a single-mode dynamic analysis, where the structural response of the flexible bridge deck can be approximated as

$$\chi(x,\ t) = \varphi(x)y(t) \tag{2}$$

where x represents the coordinate along the span-wise location; $\varphi(x)$ is the dimensionless mode shape vector; $y(t)$ is the generalized coordinate of the mode.

Assuming that the vortex-induced force is fully correlated along the span-wise direction of the bridge deck, the governing equation for the single-mode dynamic analysis is then expressed as

$$M(\ddot{y} + 2\xi_0\omega_0\dot{y} + \omega_0^2 y) = Q(t) \tag{3}$$

where M is the modal mass and Q is the generalized vortex-induced force, which can be respectively expressed as

$$M = \int_0^L m\varphi^2(x)dx \tag{4a}$$

$$Q(t) = \int_0^L F(t)\varphi(x)dx \tag{4b}$$

where m is equivalent mass of the bridge deck per unit span length; L is the length of the bridge deck. It should be mentioned that the non-fully span-wise correlation of the vortex-induced force on the flexible bridge deck is not considered in the present paper.

3. A simplified model to evaluate peak vertical VIV amplitude

An appropriate expression for the vortex-induced force F is of great significance to accurately evaluate the VIV response of a bridge deck. A physical sound modeling scheme is to simulate the nonlinear vortex-induced force with an amplitude-dependent function of the time-varying displacement and velocity of the bridge deck [e.g., 24, 34, 41, 68], which is essentially based on the describing function theory [45, 46]. Recently, Zhang et al. [34] showed that the describing function-based model can satisfactorily predict the VIV amplitudes of a rigid cylinder in a wide range of Sc

$$F = \rho U^2 D\left[KH_1^*(A,\ K)\frac{\dot{y}}{U} + K^2H_4^*(A,\ K)y + C_L(K)\sin(\omega_s t + \theta)\right] \tag{5}$$

where ρ is the air density; $K = \omega_0 D/U$ is the reduced frequency; A is the amplitude of the dimensionless displacement y/D; H_1^* and H_4^* are aerodynamic describing functions (or amplitude-dependent flutter derivatives) characterizing the motion-induced contribution in the vortex-induced force; C_L represents an aerodynamic parameter characterizing the forcing term in the vortex-induced force; $\omega_s = 2\pi S_t U/D$ (where S_t represents the Strouhal number) and θ are the circular frequency and initial phase of the forcing term, respectively. Experimental observations show that, for large-amplitude vibration responses in the lock-in range, the forcing term is negligible compared to the motion-induced force [30]. In addition, the aerodynamic stiffness term is known to have insignificant effect on the VIV response for a structure with large mass ratio (between structure and displaced air). As a result, Eq. (5) can be simplified as

$$F = \rho U^2 D\left[KH_1^*(A,\ K)\frac{\dot{y}}{U}\right] \tag{6}$$

The governing equation of the bridge deck sectional model, i.e., Eq. (1), is then expressed as

$$m(\ddot{y} + 2\xi_0\omega_0\dot{y} + \omega_0^2 y) = \rho U^2 D\left[KH_1^*(A,\ K)\frac{\dot{y}}{U}\right] \tag{7}$$

which can be re-arranged as

$$\ddot{y} + \mu\omega_0\left[\frac{Sc}{2\pi} - \frac{D}{B}H_1^*(A,\ K)\right]\dot{y} + \omega_0^2 y = 0 \tag{8}$$

where B is the deck with; $\mu = \rho BD/m$ is a dimensionless variable characterizing the mass ratio between the displaced air and the structure; $Sc = 4\pi m\xi_0/(\rho BD)$ is the Scruton number.

As indicated by Eq. (8), the key parameters that determine the VIV amplitude of a bridge deck are Sc and $H_1^*(A,\ K)$. For a pre-determined Sc, the VIV amplitude at a specific K (or reduced wind speed $U_r = 2\pi/K$) corresponds to the intersection point between the $H_1^*(A,\ K)$ curve and the horizontal line $Sc(A)$ [34]. As schematically illustrated in Fig. 2, for $Sc > Sc_1$, the $A_{\max}$ occurs at $U_{r,1}$; for $Sc_2 < Sc \leq Sc_1$, the $A_{\max}$ occurs at $U_{r,2}$; for $Sc \leq Sc_2$, the $A_{\max}$ occurs at $U_{r,3}$. Since the $A_{\max}$ occurs at different U_r for various Sc, it is generally necessary to obtain all the VIV amplitudes in the entire lock-in range to determine the $A_{\max}$ for a specific bridge deck. On the other hand, it is useful to develop a simplified model in order to more conveniently evaluate the

$A_{\max}$ of a bridge deck at various Sc. To this end, the maximum value of $H_1^*(A,\ K)$ at various K (or U_r) can be merged together to form a $H_{1,\ \max}^*(A)$ curve, as illustrated by the red line in Fig. 2. It is noted that Fig. 2 is a schematic diagram to show the determination of $H_{1,\ \max}^*(A)$ based on $H_1^*(A,\ K)$ at various U_r. Practically, $H_1^*(A,\ K)$ at more U_r (i.e., preferably distributed densely in the entire lock-in range) should be included. It is noted that $H_{1,\ \max}^*(A)$ is the upper envelop of $H_1^*(A,\ K)$, and $H_{1,\ \max}^*(A)$ reflects the maximum negative aerodynamic damping versus A in the lock-in range. Accordingly, the following expression for the vortex-induced force can be utilized to conveniently evaluate the $A_{\max}$ of a bridge deck at various Sc

$$F = \rho U^2 D\left[K H_{1,\ \max}^*(A)\frac{\dot{y}}{U} \right] \tag{9}$$

The governing equations for the VIVs of a bridge deck sectional model and a flexible bridge deck respectively become

$$m(\dot{y} + 2\xi_0\omega_0\dot{y} + \omega_0^2 y) = \rho U^2 D\left[K H_{1,\ \max}^*(A)\frac{\dot{y}}{U} \right] \tag{10a}$$

$$M(\ddot{y} + 2\xi_0\omega_0\dot{y} + \omega_0^2 y) = \rho U^2 D\left[K\int_0^L H_{1,\ \max}^*(A)\frac{\dot{y}}{U}\varphi^2(x)dx \right] \tag{10b}$$

Once the $H_{1,\ \max}^*(A)$ is identified for a cross-section, the peak VIV amplitudes for rigid and flexible bridge decks with the same cross-section at various Sc can be conveniently obtained according to Eqs. (10a) and (10b), respectively. For a rigid bridge deck, it is obvious from Fig. 2 that the $A_{\max}$ at any Sc determined by $H_{1,\ \max}^*(A)$ and that determined by the describing functions are the same. Therefore, $A_{\max}$ calculated by Eq. (10a) are consistent with those calculated by the describing function-based model. However, it will be demonstrated later that, for a flexible bridge, Eq. (10b) always results in slightly conservative (i.e., larger) $A_{\max}$ than the describing function-based model. The new model [i.e., Eq. (9)] is more convenient than the describing function-based model since the new model can directly obtain the $A_{\max}$ at various Sc without calculating all the VIV amplitudes in the entire lock-in range. Furthermore, the new model is more practical for engineers in the bridge engineering community since it contains a single group of aerodynamic parameters which don't vary with the reduced wind speed. The identification of $H_{1,\ \max}^{*}(A)$ will be discussed in the following section. A similar model may be utilized to calculate the peak torsional VIV amplitude of a bridge deck, while the torsional cases are not considered in the present paper.

It is worth mentioning that there exist some other mathematical models to directly calculate the peak VIV amplitude [47, 48] of a line-like structure without calculating all the VIV amplitudes in the entire lock-in range. The models in [47] and [48] are indeed special cases of the present model: in the former one, $H_{1,\ \max}^{*}$ is assumed as a linear function of $1/A$; in the latter one, $H_{1,\ \max}^{*}$ is fitted as an explicit function of A based on the aerodynamic damping envelope of a circular cylinder. In the following part, these models will not be further discussed since none of them can outperform the present model.

4. Identification of $H_{1,\ \max}^{*}(A)$ based on sectional model tests

As mentioned in the preceding section, $H_{1,\ \max}^{*}(A)$ is the upper envelop of $H_1^{*}(A,\ K)$ and hence it is necessary to obtain the $H_1^{*}(A,\ K)$ in the A and K ranges of interests in order to determine $H_{1,\ \max}^{*}(A)$. $H_1^{*}(A,\ K)$ is indeed an improved version of the traditional flutter derivative [49] with amplitude-dependent feature. Accordingly, the existing methods for extracting flutter derivatives based on sectional model tests (or numerical simulations) may be extended to identify $H_1^{*}(A,\ K)$ [50-52]. The common experimentally or numerically forced vibration-based method (with sinusoidal displacement input) is time consuming because for a specific K, wind tunnel tests (or numerical simulations) with a number of different vibration amplitudes are required. Displacement inputs with continuously varying amplitudes may be utilized in forced vibrations to reduce the experimental/computational cost of $H_1^{*}(A,\ K)$ identification [53].

On the other hand, since the VIV performance a bridge deck is commonly studied through free vibration wind tunnel tests, in which only the decay/growth-to-resonance displacement signals are recorded, it is of significant interests to extract $H_1^{*}(A,\ K)$ based on the displacement signals recorded in free vibration tests.

Several procedures [34, 39, 41, 54] have been developed to extract $H_1^*(A, K)$ according to the amplitude-dependent damping ratios of the VIV displacement signals. The $H_1^*(A, K)$ in the A and K ranges of interests can be identified based on the obtained VIV displacement signals at a single Sc.

Furthermore, $H_1^*(A, K)$ for a specific K can be extracted based on the VIV steady amplitudes at various Sc. At the VIV steady amplitude, the equivalent negative aerodynamic damping ratio balances the mechanical damping ratio. Accordingly, H_1^* at the VIV steady amplitude for a specific Sc can be obtained as

$$H_1^* = \frac{Sc}{2\pi}\frac{B}{D} \tag{11}$$

Due to the increasing application of advanced additional damping devices in wind tunnel tests, e.g., the eddy current damper [55, 56], it is now convenient to adjust the mechanical damping ratio (and hence Sc) during wind tunnel tests. As a result, for a specific K, the A at various Sc can be obtained conveniently, and hence the H_1^* at various A can be determined according to Eq. (11). Finally, the $H_1^*(A, K)$ curve for this specific K can be obtained through curve fitting based on the available values of H_1^* at various A. In practical applications, the steady amplitudes-based method and the transient response-based method can be utilized in combination to improve the identification accuracy and efficiency.

Once $H_1^*(A, K)$ are obtained in the A and K ranges of interests, $H_{1,\ \max}^*(A)$ can be further determined through curve fitting based on the available data on the upper boundary of $H_1^*(A, K)$. In the present paper, the following expression is suggested since it works satisfactorily for several cross-sections

$$H_{1,\ \max}^*(A) = P_0 + \sum_{i=1}^{n} P_i \exp(-A/c_i) \tag{12}$$

where P_0, P_i, and c_i (i =1 ~ n) are constants of the fitting results. It is found that n = 1 or 2 is sufficiently accurate for the cross-sections considered in this paper.

5. Numerical examples

To validate the simulation accuracy of the proposed model, numerical examples involving the VIV analyses of a rigid rectangular cylinder and a bridge deck sectional model are presented in this section. The proposed model is then utilized to calculate the $A_{\max}$ of two flexible bridge decks at various ξ_0.

5.1. VIV of a rigid rectangular cylinder

The first example analyzes the vertical VIV of a rigid rectangular cylinder with side ratio $B/D = 4$ (B is the deck width). The aerodynamic performance of this cross-section is of significant interests in the wind engineering community because the cross-section is widely adopted in various types of structures and can be regarded as a simplified bridge deck section. The experimental VIV responses in [33] are utilized to extract the $H_1^*(A, K)$ and $H_{1,\max}^*(A)$ of the considered cross-section. The main modal parameters of the wind tunnel tests are $m = 7.09 \sim 7.29$ kg/m, $\omega_0 = 49.45 \sim 50.07$ rad/s, $\rho = 1.19 \sim 1.22$ kg/m^3, and $D = 0.075$ m; ξ_0 is varied in 0.058% ~2.34%, resulting in a $Sc = 4\pi m\xi_0/(\rho BD)$ range of 1.9 ~ 78.1. The initial wind angle of attack is $\alpha_0 = 0°$. The lock-in ranges and VIV amplitudes at various $Sc = 4\pi m\xi_0/(\rho BD)$ are presented in Fig. 3(a), in which the $A_{\max}$ are highlighted by red star markers. It is noted that the $A_{\max}$ at various Sc occur at different U_r. The decay-to-resonance displacement signal for $Sc = 78.1$, $U_r = 8.14$ (corresponds to the $A_{\max}$ at $Sc = 78.1$) is shown in Fig. 3(b) as a representative. The displacement signal decays after a large initial excitation and finally becomes steady limit cycle oscillation with increasing time. The signal will be utilized to identify the $H_1^*(A, K)$ for $U_r = 8.14$.

Fig. 4 presents the $H_1^*(A, K)$ results for $U_r = 8.14$ identified based on the steady amplitudes at various Sc and based on the decay-to-resonance displacement signal at $Sc = 78.1$. It is observed that the results of the two methods agree satisfactorily, indicating that the $H_1^*(A, K)$ [and hence $H_{1,\max}^*(A)$] can be either identified based on the VIV decay-to-resonance and/or grow-to-resonance signals at a single Sc, or based on the VIV steady amplitudes at various Sc. However, the identification results of the two methods exhibit slight discrepancies for $A > 0.03$. The discrepancies may be mainly ascribed to the identification errors of the transient response-based method, where the fitted instantaneous amplitude of the displacement signal may be not accurate enough to extract the instantaneous damping ratio for the rapidly decaying response within $Ut/D < 50$ in Fig. 3 [34]. The VIV amplitudes at $U_r = 8.14$ calculated by the two sets of $H_1^*(A, K)$ are shown in Fig. 5 together with the experimental measurements in [33]. The satisfactory agreements between the experimental and calculated amplitudes prove that the identification results of $H_1^*(A, K)$ are fairly accurate. It is noted that since the slope of the $H_1^*(A, K)$ curve is very small for $A > 0.03$, the slight identification error in $H_1^*(A, K)$ leads to remarkable errors in the simulated VIV amplitudes. In addition, the $H_1^*(A, K)$ result based on steady VIV amplitudes seems more reliable since the predicted VIV amplitudes are more accurate.

H_1^* for various U_r are identified based on the VIV steady amplitudes in Fig. 3(a), and the identification results are presented in Fig. 6. It is noted that, for different A, H_1^* achieves the maximum value at different U_r, and hence the envelope [i.e., $H_{1,\ \max}^*(A)$] cannot be determined by the H_1^* at any single U_r. $H_{1,\ \max}^*$ is fitted using Eq. (12) based on the available data on the upper boundary of H_1^*. The fitting result in Fig. 6 suggests that the format of Eq. (12) works very well for the $B/D = 4$ rectangular section. In this example, $n = 2$ is used, since further increasing n does not contribute to a betting fitting. In addition, a polynomial with linear and third order nonlinear terms (which represents the amplitude-dependent aerodynamic damping curve deduced from the widely-used van der Pol-type model [25, 29]) is also utilized to fit the experimental boundary of H_1^*. The fitting result in Fig. 6 suggests that the van der Pol-type model fails to correctly capture the nonlinear aerodynamic damping of the VIV system.

The $A_{\max}$ of the rectangular cylinder at various Sc are calculated based on the two fitted $H_{1,\ \max}^*$ curves in Fig 6, and the results are presented together with available experimental measurements [32, 33, 41, 57-61] in Fig. 7. The main modal parameters of the wind tunnel tests in these literatures are summarized in Table 1. For a rigid cylinder, the $A_{\max}$ at various Sc calculated by the describing function-based model are consistent with those calculated by the proposed model, and hence the describing function-based results are not shown for brevity. It can be seen that the data of various tests with different modal parameters collapse very well to the curve calculated by the proposed model, while the van der Pol-type model fails to simulate the A_{max} in the considered Sc range. The results suggest that the proposed model is capable of accurately and conveniently predicting the peak VIV amplitudes of a bridge deck sectional model at various mass-damping conditions.

It should be stated that the very good predicative capability of the proposed model shown in Fig. 7 are indeed because the experimental data used to identify the aerodynamic parameters are enough to characterize the VIV behavior of the rigid cylinder, i.e., the data in the same range of Sc are used to identify the aerodynamic parameters and validate the mathematical models. If the aerodynamic parameters of the transient response-based method are used to calculate the steady amplitudes (i.e., if the aerodynamic parameters are identified based on the VIV displacement histories at a single Sc, and then used to predict the steady amplitudes at other Sc), the accuracy of the model may decrease, as shown in Fig. 5. In subsection 5.2, it will be further proved that, with the $H^*_{1,\ \max}$ identified based on the VIV displacement signals at a signal Sc, the proposed model is capable of conveniently predicting the peak VIV amplitudes at other Sc. Indeed, for a rigid cylinder, it is unnecessary to calculate the VIV amplitudes by a mathematical model in case that the experimental results at various Sc are available. However, for of a flexible cylinder, a mathematical model is always necessary since the experimental results based on a rigid sectional model cannot consider the effect of mode shape.

5.2. VIV of a bridge deck sectional model

The second example analyzes the vertical VIV of a centrally slotted box deck sectional model tested in [38]. Geometry of the considered cross-section is available in Fig. 1(b) of [38]. The main modal parameters of the wind tunnel tests are m = 50.45 kg/m, ω_0 = 27.38 rad/s, B = 1.70 m, D = 0.175 m, and ξ_0 = 0.26% and 0.45% (Sc = 4.5 and 7.8). The initial wind angle of attack is α_0 =0°. The lock-in ranges and VIV amplitudes at two Sc are presented in Fig. 8, in which the A_{max} are highlighted by red star markers. The VIV displacement signals are not shown for brevity.

H^*_1 for various U_r are identified based on the VIV displacement signals at Sc = 4.5, and the identification results are presented in Fig. 9. $H^*_{1,\ \max}$ is fitted using Eq. (12) based on the available data on the upper boundary of H^*_1. The fitting result in Fig. 9 suggests that the format of Eq. (12) works very well for the slotted box deck section.

The $A_{\max}$ of the rectangular cylinder at various Sc are calculated based on the two fitted $H^*_{1,\ \max}$ curves in Fig 9, and the results are presented together with the experimental measurements in Fig. 10. The comparison again suggests that the proposed model is capable of accurately and conveniently predicting the peak VIV amplitudes of a bridge deck sectional model at various mass-damping conditions.

5.3. VIVs of two flexible bridge decks

After validating the capability of the proposed model in calculating the $A_{\max}$ of bridge deck sectional models at various Sc, the model is then utilized to calculate the $A_{\max}$ of two flexible bridge decks at various ξ_0. The example bridge decks are a cable-stayed bridge deck with span arrangement of 100 × 2 + 300 + 1088 + 300 + 100 × 2 m, and a suspension bridge deck with span arrangement of 576 + 1650 m. The modal frequencies and modal masses (ω_0 and m) of the first five vertical modes of two bridge decks are calculated by previously developed finite element models (see Appendix), as shown in Tables 2 and 3, respectively, and the corresponding mode shapes [denoted as $\varphi_i(x)$ (i = 1 to 5)] are presented in Figs. 11 and 12, respectively. Since the aerodynamic parameters for the example bridge decks are unavailable, they are supposed to have the same $H^*_1(A,\ K)$ and $H^*_{1,\ \max}$ curves with those of the B/D = 4 rectangular section, and it is assumed that B = 24 m and D = 6 m in the following analyses.

Since the present model is a simplified form of the describing function-based model, it is useful to compare the results of the two models in order to partly validate the capability of the present model in calculating the $A_{\max}$ for flexible bridge decks. The $A_{\max}$ for two bridge decks at various ξ_0 are calculated using the present model, as shown in Figs. 13(a) and 14(a), respectively. For two selected modes of each bridge deck, the $A_{\max}$ at various ξ_0 are also calculated using the describing function-based model for comparison. The describing function-based results can be also calculated for other modes, while the results are not given herein for brevity. It is noted that the results of the present model are slightly larger than those of the describing function-based model. The phenomenon can be explained as follows: for a flexible bridge deck, the vibration amplitude varies continuously along its span-wise direction; to calculate the $A_{\max}$ for a specific Sc, the H_1^* curve at the U_r that $A_{\max}$ occurs should be utilized in the expression of the vortex-induced force (indeed, the describing function-based model correctly expresses the vortex-induced force with the H_1^* curve at this specific U_r); however, the present model utilizes the envelope of H_1^* [i.e., $H_{1,\max}^*(A)$] to calculate $A_{\max}$, and hence the negative aerodynamic damping (as well as the absorbed energy) at some span-wise segments is overestimated; as a result, the present model always leads to a slightly overestimated $A_{\max}$ than the describing function-based model. For a case with lower ξ_0 (and hence larger $A_{\max}$), the aerodynamic damping of longer segments of the flexible bridge deck is overestimated, and hence the error of the present model becomes larger with decreasing ξ_0. The results in Figs. 13(a) and 14(a) and the preceding discussions suggest that the present model always results in slightly conservative $A_{\max}$ in the VIV analysis of flexible bridges. Compared with the results of the describing function-based model, the largest relative errors of the present model for the cable-stayed bridge deck and the suspension bridge deck are 11.7% and 7.3%, respectively. From an engineering point of view, the results of the present model are considered to be acceptable for the example bridge decks.

It is well known that the VIV amplitude of a flexible bridge deck deviates from its rigid counterpart due to the effect of the mode shape and the non-fully span-wise correlation of the vortex-induced force [62-66]. For fully correlated cases analyzed in this example, the ratio between the $A_{\max}$ of a flexible bridge deck to that of a rigid one is often known as a mode shape correction factor λ. For two selected modes of each bridge deck, the λ at various ξ_0 are calculated by the conventional van der Pol-type model, the present model, and the describing function-based model, as shown in Figs. 13(b) and 14(b), respectively. It is noted that the λ determined by the van der Pol-type model is independent of ξ_0, while those determined by the present model and the describing function-based model decrease with increasing ξ_0. The results of the present model are slightly higher than those of the describing function-based model since the $A_{\max}$ determined by the present model is higher, as shown in Figs. 13(a) and 14(a). On the other hand, the results of the van der Pol-type model are remarkably lower than those of the other two models. To explain these observations, the effective aerodynamic damping ratio ξ_{aero} for Mode 1 of the cable-stayed bridge deck calculated by the present model [i.e., $\rho D^2 H_{1,\ \max}^{*}(A)/(2m)$], and the ξ_{aero} at $U_r = 8.14$ and 8.66 calculated by the describing function-based model and the van der Pol-type model (with aerodynamic parameters given in [33]) are shown in Fig. 15. As discussed earlier, the ξ_{aero} calculated by the describing function-based model can be taken as the reference values, while the present model slightly overestimates the negative aerodynamic damping ratios in some amplitude ranges. It can be seen that the van der Pol-type can only accurately reproduce the aerodynamic damping ratios in a very limited amplitude range, while highly underestimates the negative aerodynamic damping ratios in other amplitude ranges. As a result, the van der Pol-type model underestimates the negative aerodynamic damping ratios (as well as the absorbed energy) at some span-wise segments of the flexible bridge deck, and hence yields underestimated $A_{\max}$ and λ. For a case with lower ξ_0 (and hence larger $A_{\max}$), the aerodynamic damping ratios of longer segments of the flexible bridge deck are underestimated, and hence the error of the van der Pol-type model becomes larger with decreasing ξ_0. The results in Figs. 13(b) and 14(b) and the preceding discussions suggest that the $A_{\max}$ of a flexible bridge deck calculated by the van der Pol-type is unsafe, and the error increases with decreasing the mechanical damping ratio of the bridge deck.

6. Conclusions

The paper develops a simplified model to conveniently evaluate the peak VIV amplitudes of a bridge deck at various mass-damping conditions. The key innovation of the new model is the introduction of an envelope curve of the aerodynamic describing functions, i.e., the $H_{1,\ \max}^{*}(A)$ curve, which determines the maximum negative aerodynamic damping versus vibration amplitude in the lock-in range. The new model is more practical for engineers in the bridge engineering community since it only contains a single group of aerodynamic parameters which don't vary with the reduced wind speed. The $H_{1,\max}^{*}(A)$ curve can be either identified based on the VIV decay-to-resonance and/or grow-to-resonance signals at a single mass-damping condition, or based on the VIV steady amplitudes at various mass-damping conditions. Numerical examples involving the VIV analyses of a rigid rectangular cylinder and a bridge deck sectional model are utilized to validate the simulation accuracy of the proposed model, and the model is applied to calculate the peak VIV amplitudes of two flexible bridge decks at various mechanical damping levels. Some major conclusions are summarized as follows:

(1) The proposed model is capable of accurately and conveniently predicting the peak VIV amplitudes of a bridge deck sectional model at various mass-damping conditions without calculating all the VIV amplitudes in the entire lock-in range;

(2) For a flexible bridge deck, the peak VIV amplitude calculated by the proposed model is slightly conservative due to the overestimated negative aerodynamic damping at some span-wise segments of the bridge deck;

(3) The conventional van der Pol-type model may remarkably underestimate the peak VIV amplitude for a flexible bridge deck.

Author's Contributions

Mingjie Zhang: Conceptualization, methodology, data analysis, writing original draft. **Fuyou Xu:** Conceptualization, methodology, data analysis, writing original draft. **Haiyan Yu:** writing original draft, validation.

Declaration of Competing Interest

The authors declare that they have no known competing financial interests or personal relationships that could have appeared to influence the work reported in this paper.

Acknowledgements

This research was supported by the National Natural Science Foundation of China, grant number 51678115 and 51978130.

Appendix

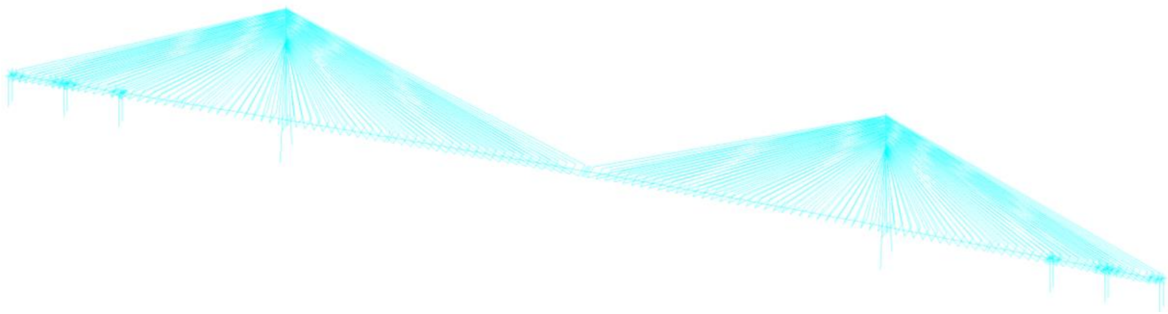

Fig. A1. Finite element model of a cable-stayed bridge

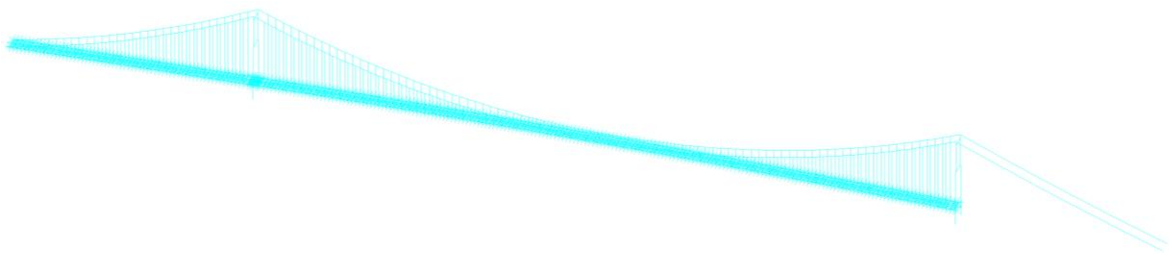

Fig. A2. Finite element model of a suspension bridge

References

[1] Fujino, Y., Yoshida, Y., 2002. Wind-induced vibration and control of Trans-Tokyo Bay crossing bridge. J. Struct. Eng. 128(8), 1012-1025.

[2] Weber, F., Maślanka, M., 2012. Frequency and damping adaptation of a TMD with controlled MR damper. Smart Mater. Struct. 21(5), 055011.

[3] Seo, J. W., Kim, H. K., Park, J., Kim, K. T., Kim, G. N., 2013. Interference effect on vortex-induced vibration in a parallel twin cable-stayed bridge. J. Wind Eng. Ind. Aerodyn. 116, 7-20.

[4] Li, H., Laima, S., Zhang, Q., Li, N., Liu, Z., 2014. Field monitoring and validation of vortex-induced vibrations of a long-span suspension bridge. J. Wind Eng. Ind. Aerodyn. 124, 54-67.

[5] Li, H., Laima, S., Ou, J., Zhao, X., Zhou, W., Yu, Y., Li, N., Liu, Z., 2011. Investigation of vortex-induced vibration of a suspension bridge with two separated steel box girders based on field measurements. Eng. Struct. 33(6), 1894-1907.

[6] Li, H., Laima, S., Jing, H., 2014. Reynolds number effects on aerodynamic characteristics and vortex-induced vibration of a twin-box girder. J Fluids Struct. 50, 358-375.

[7] Frandsen, J. B., 2001. Simultaneous pressures and accelerations measured full-scale on the Great Belt East suspension bridge. J. Wind Eng. Ind. Aerodyn. 89(1), 95-129.

[8] Sarwar, M. W., Ishihara, T., 2010. Numerical study on suppression of vortex-induced vibrations of box girder bridge section by aerodynamic countermeasures. J. Wind Eng. Ind. Aerodyn. 98(12), 701-711.

[9] Martins, F. A. C., Avila, J. P. J., 2019. Effects of the Reynolds number and structural damping on vortex-induced vibrations of elastically-mounted rigid cylinder. Int. J. of Mech. Sci. 156, 235-249.

[10] Xu, F., Ying, X., Li, Y., Zhang, M., 2016. Experimental explorations of the torsional vortex-induced vibrations of a bridge deck. J. of Bridge Eng. 21(12), 04016093.

[11] Xin, D., Zhang, H., Ou, J., 2018. Experimental study on mitigating vortex-induced vibration of a bridge by using passive vortex generators. J. Wind Eng. Ind. Aerodyn. 175, 100-110.

[12] Ma, C. M., Wang, J. X., Li, Q. S., Qin, H., Liao, H. L., 2018. Vortex-induced vibration performance and suppression mechanism for a long suspension bridge with wide twin-box girder. J. Struct. Eng. 144(11), 04018202.

[13] Avila-Sanchez, S., Lopez-Garcia, O., Cuerva, A., Meseguer, J., 2017. Assesment of the transverse galloping stability of a railway overhead located above a railway bridge. Int. J. of Mech. Sci. 131, 649-662.

[14] Zhang, M., Xu, F., Ying, X., 2017. Experimental investigations on the nonlinear torsional flutter of a bridge deck. J. Bridge Eng. 22(8), 04017048.

[15] Wu, T., Kareem, A., 2012. An overview of vortex-induced vibration (VIV) of bridge decks. Front. Struct. Civ. Eng. 6(4), 335-347.

[16] Hartlen, R. T., Currie, I. G., 1970. Lift-oscillator model of vortex-induced vibration. J. Eng. Mech. Div. 96(5), 577-591.

[17] Facchinetti, M. L., De Langre, E., Biolley, F., 2004. Coupling of structure and wake oscillators in vortex-induced vibrations. J. Fluids Struct. 19(2), 123-140.

[18] Kurushina, V., Pavlovskaia, E., Postnikov, A., Wiercigroch, M., 2018. Calibration and comparison of VIV wake oscillator models for low mass ratio structures. Int. J. of Mech. Sci. 142, 547-560.

[19] Postnikov, A., Pavlovskaia, E., Wiercigroch, M., 2017. 2DOF CFD calibrated wake oscillator model to investigate vortex-induced vibrations. Int. J. of Mech. Sci. 127, 176-190.

[20] Qu, Y., Metrikine, A. V., 2020. A wake oscillator model with nonlinear coupling for the vortex-induced vibration of a rigid cylinder constrained to vibrate in the cross-flow direction. J. Sound Vib. 469, 115-161.

[21] Yang, W., Ai, Z., Zhang, X., Chang, X., Gou, R., 2018. Nonlinear dynamics of three-dimensional vortex-induced vibration prediction model for a flexible fluid-conveying pipe. Int. J. of Mech. Sci. 138, 99-109.

[22] Sun, W., Jo, S., Seok, J., 2019. Development of the optimal bluff body for wind energy harvesting using the synergetic effect of coupled vortex induced vibration and galloping phenomena. Int. J. of Mech. Sci. 156, 435-445.

[23] Sarpkaya, T., 1979. Vortex-induced oscillations: a selective review. ASME. J. Appl. Mech. 46(2), 241-258.

[24] Morse, T. L., and Williamson, C. H. K., 2009. Prediction of vortex-induced vibration response by employing controlled motion. J Fluid Mech. 634, 5-39.

[25] Vickery, B. J., Basu, R. I., 1983. Across-wind vibrations of structures of circular cross-section. Part I. Development of a mathematical model for two-dimensional conditions. J. Wind Eng. Ind. Aerodyn. 12(1), 49-73.

[26] Morse, T. L., Williamson, C. H. K., 2010. Steady, unsteady and transient vortex-induced vibration predicted using controlled motion data. J Fluid Mech. 649, 429.

[27] Ma, C. M., Liu, Y. Z., Li, Q. S., Liao, H. L., 2018. Prediction and explanation of the aeroelastic behavior of a square-section cylinder via forced vibration. J. Wind Eng. Ind. Aerodyn. 176, 78-86.

[28] Han, Q., Ma, Y., Xu, W., Fan, D., Wang, E., 2018. Hydrodynamic characteristics of an inclined slender flexible cylinder subjected to vortex-induced vibration. Int. J. of Mech. Sci. 148, 352-365.

[29] Scanlan, R. H., 1981. State-of-the-art methods for calculating flutter, vortex-induced, and buffeting response of bridge structures. Technical Rep. FHWA/RD-80/050, National Technical Information Service, Springfield, VA.

[30] Ehsan, F., Scanlan, R. H., 1990. Vortex-induced vibrations of flexible bridges. J. Eng. Mech. 116(6). 1392-1411.

[31] Gupta, H., Sarkar, P. P., Mehta, K. C., 1996. Identification of vortex-induced-response parameters in time domain. J. Eng. Mech. 122(11), 1031-1037.

[32] Marra, A. M., Mannini, C., Bartoli, G., 2011. Van der Pol-type equation for modeling vortex-induced oscillations of bridge decks. J. Wind Eng. Ind. Aerodyn. 99(6-7), 776-785.

[33] Marra, A. M., Mannini, C., Bartoli, G., 2015. Measurements and improved model of vortex-induced vibration for an elongated rectangular cylinder. J. Wind Eng. Ind. Aerodyn. 147, 358-367.

[34] Zhang, M., Wu, T., Xu, F., 2019. Vortex-induced vibration of bridge decks: Describing function-based model. J. Wind Eng. Ind. Aerodyn. 195, 104-116.

[35] Goswami, I., Scanlan, R. H., Jones, N. P., 1993. Vortex-induced vibration of circular cylinders. I: experimental data. J. Eng. Mech. 119(11), 2270-2287.

[36] Larsen, A., 1995. A generalized model for assessment of vortex-induced vibrations of flexible structures. J. Wind Eng. Ind. Aerodyn. 57(2-3), 281-294.

[37] Zhu, L. D., Meng, X. L., Guo, Z. S., 2013. Nonlinear mathematical model of vortex-induced vertical force on a flat closed-box bridge deck. J. Wind Eng. Ind. Aerodyn. 122, 69-82.

[38] Zhu, L. D., Meng, X. L., Du, L. Q., Ding, M. C., 2017. A simplified nonlinear model of vertical vortex-induced force on box decks for predicting stable amplitudes of vortex-induced vibrations. Engineering, 3(6), 854-862.

[39] Xu, K., Ge, Y., Zhao, L., Du, X., 2018. Calculating vortex-induced vibration of bridge decks at different mass-damping conditions. J. Bridge Eng. 23(3), 04017149.

[40] Wu, T., Kareem, A., 2013. Vortex-induced vibration of bridge decks: Volterra series-based model. J. Eng. Mech. 139(12), 1831-1843.

[41] Mashnad, M., Jones, N. P., 2014. A model for vortex-induced vibration analysis of long-span bridges. J. Wind Eng. Ind. Aerodyn. 134, 96-108.

[42] Xu, K., Zhao, L., Ge, Y., 2017. Reduced-order modeling and calculation of vortex-induced vibration for large-span bridges. J. Wind Eng. Ind. Aerodyn. 167, 228-241.

[43] Li, S., Laima, S., Li, H., 2018. Data-driven modeling of vortex-induced vibration of a long-span suspension bridge using decision tree learning and support vector regression. J. Wind Eng. Ind. Aerodyn. 172, 196-211.

[44] Xu, K., Ge, Y., Zhao, L., 2020. Quantitative evaluation of empirical models of vortex-induced vibration of bridge decks through sectional model wind tunnel testing. Eng. Struct. 219, 110860.

[45] Peyton-Jones, J. C., Billings, S. A., 1991. Describing functions, Volterra series, and the analysis of non-linear systems in the frequency domain. Int. J. Control 53(4), 871-887.

[46] Zhang, M, Xu, F, Wu, T, Zhang, Z., 2020. Postflutter analysis of bridge decks using aerodynamic describing functions. J. Bridge Eng. 25(8): 04020046.

[47] HEPC (Hanshin Expressway Public Corporation), 1984. Aerodynamic design method on wind resistant design.

[48] Lupi, F., Niemann, H. J., Höffer, R., 2018. Aerodynamic damping model in vortex-induced vibrations for wind engineering applications. J. Wind Eng. Ind. Aerodyn., 174, 281-295.

[49] Scanlan, R. H., Tomko, J. J., 1971. Airfoil and bridge deck flutter derivatives. J. Eng. Mech. 97(6), 1717-1737.

[50] Diana, G., Resta, F., Belloli, M., Rocchi, D., 2006. On the vortex shedding forcing on suspension bridge deck. J. Wind Eng. Ind. Aerodyn. 94(5), 341-363.

[51] Noguchi, K., Ito. Y., Yagi, T., 2020. Numerical evaluation of vortex-induced vibration amplitude of a box girder bridge using forced oscillation method. J. Wind Eng. Ind. Aerodyn.

[52] Zhang, M., Xu, F., Zhang, Z., Ying, X., 2019. Energy budget analysis and engineering modeling of post-flutter limit cycle oscillation of a bridge deck. J. Wind Eng. Ind. Aerodyn. 188, 410-420.

[53] Xu, F., Ying, X., Zhang, Z., 2016. Effects of exponentially modified sinusoidal oscillation and amplitude on bridge deck flutter derivatives. J. Bridge Eng. 21(5), 06016001.

[54] Zhang, M., Xu, F., 2018. Nonlinear vibration characteristics of bridge deck section models in still air. J. Bridge Eng. 23(9), 04018059.

[55] Larose, G. L., Larsen, A., Svensson, E., 1995. Modelling of tuned mass dampers for wind-tunnel tests on a full-bridge aeroelastic model. J. Wind Eng. Ind. Aerodyn. 54, 427-437.

[56] Huang, Z. W., Hua, X. G., Chen, Z. Q., Niu, H. W., 2018. Modeling, testing, and validation of an eddy current damper for structural vibration control. J. Aerospace Eng. 31(5), 04018063.

[57] Washizu, K., Ohya, A., Otsuki, Y., Fujii, K., 1978. Aeroelastic instability of rectangular cylinders in a heaving mode. J. Sound Vib. 59(2), 195-210.

[58] Miyata, T., Miyazaki, M., Yamada, H., 1983. Pressure distribution measurements for wind induced vibrations of box girder bridges. J. Wind Eng. Ind. Aerodyn. 14(1-3), 223-234.

[59] Scanlan, R. H., 1998. Bridge flutter derivatives at vortex lock-in. J. Struct. Eng. 124(4), 450-458.

[60] Sun, Y., Li, M., Li, M., Liao, H., 2019. Spanwise correlation of vortex-induced forces on typical bluff bodies. J. Wind Eng. Ind. Aerodyn. 189, 186-197.

[61] Shimada, K., Ishihara, T., 2012. Predictability of unsteady two-dimensional k-ε model on the aerodynamic instabilities of some rectangular prisms. J. Fluid. Struct. 28, 20-39.

[62] Irwin P. A., 1998. The role of wind tunnel modeling in the prediction of wind effects on bridges. Bridge aerodynamic-proceedings of the international symposium on advances in bridge aerodynamics, Rotterdam.

[63] Macdonald J, Irwin P. A, Fletcher M., 2002. Vortex-induced vibrations of the Second Severn Cross cable-stayed bridge-full-scale and wind tunnel measurements. Proc ICE: Struct Build. 152, 123-134.

[64] Zhou, S., Hua, X. G., Chen, Z. Q., Chen, W., 2017. Experimental investigation of correction factor for VIV amplitude of flexible bridges from an aeroelastic model and its 1: 1 section model. Eng. Struct. 141, 263-271.

[65] Zhang, Z., Ge, Y., Chen, Z., 2014. Vortex-induced oscillations of bridges: theoretical linkages between sectional model tests and full bridge responses. Wind Struct. 19(3), 233-247.

[66] Xu, F., Ma, Z., Zeng, H., Zhang, M., Wang, X., Wang, M., Zhang, Z., 2020. A new method for studying wind engineering of bridges: Large-scale aeroelastic model test in natural wind. J. Wind Eng. Ind. Aerodyn. 202, 104234.

[67] Zhang, M., Xu, F., Øiseth, O., 2020. Aerodynamic damping models for vortex-induced vibration of a rectangular 4: 1 cylinder: Comparison of modeling schemes. J. Wind Eng. Ind. Aerodyn. 205, 104321.

[68] Zhang, M., Xu, F., Han, Y., 2020. Assessment of wind-induced nonlinear post-critical performance of bridge decks. J. Wind Eng. Ind. Aerodyn. 203, 104251.

[69] https://www.youtube.com/watch?v=HBEHPNFmFQ0, last accessed on Sep 20, 2020.

Table 1. Modal parameters of B/D = 4 rectangular cylinders in literatures

Literature	B (m)	D (m)	m (kg/m)	ω_0 (rad/s)	Sc
Marra et al. [32]	0.3	0.075	6.09	84.4	6.0
Marra et al. [33]	0.3	0.075	7.30	49.5	1.9 ~ 78.1
Mashnad and Jones [41]	0.152	0.038	2.52	21.7	11.9
Washizu et al. [57]	0.4	0.1	un	un	2.0
Miyata et al. [58]	un	un	un	un	3.0
Scanlan [59]	0.38	0.095	7.80	un	3.2, 8.1, 9.7
Sun et al. [60]	0.4	0.1	10.31	23.8	12.7, 29.1, 52.4
Shimada and Ishihara [61]	0.12	0.03	0.85	64.7	3.2

un: unavailable

Table 2. Modal frequencies and modal masses of a cable-stayed bridge deck

Mode	ω_0 (rad/s)	m (t/m)
1	1.245	30.70
2	1.519	31.11
3	2.149	33.60
4	2.530	35.41
5	2.837	38.92

Table 3. Modal frequencies and modal masses of a suspension bridge deck

Mode	ω_0 (rad/s)	m (t/m)
1	0.638	26.68
2	0.838	26.08
3	1.126	25.35
4	1.167	26.43
5	1.447	25.66

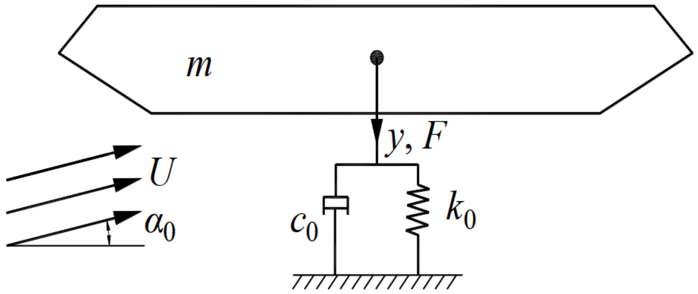

Fig. 1. Schematic diagram of a spring-suspended bridge deck sectional model immersed in two-dimensional flow. m is the mass per unit span length, k_0 is the spring stiffness constant, c_0 is the mechanical damping coefficient, U is the mean wind speed, α_0 is the initial wind angle of attack; y is the vertical displacement; F is the vortex-induced force acting on the bridge deck per unit span length, which is to be modeled in this paper.

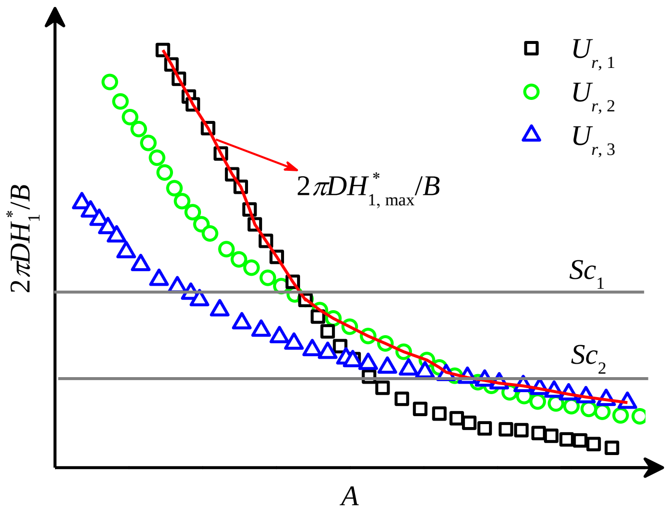

Fig. 2. Schematic diagram of aerodynamic describing functions $H_1^*(A, K)$ and aerodynamic envelope $H^*_{1,\max}(A)$ (red line). A is the dimensionless vibration amplitude, $K = \omega_0 D/U$ is the reduced frequency, where ω_0 represents the natural circular frequency, D is the depth of the deck cross-section, U is the mean wind speed. For a specific mass-damping condition Sc, the steady VIV amplitude at a specific reduced wind speed $U_r = U/(\omega_0 D/2\pi)$ corresponds to the intersection point between the $H_1^*(A, K)$ curve and the horizontal line $Sc(A)$; the intersection point between the $H^*_{1,\max}(A)$ curve and the horizontal line $Sc(A)$ determines the peak VIV amplitude.

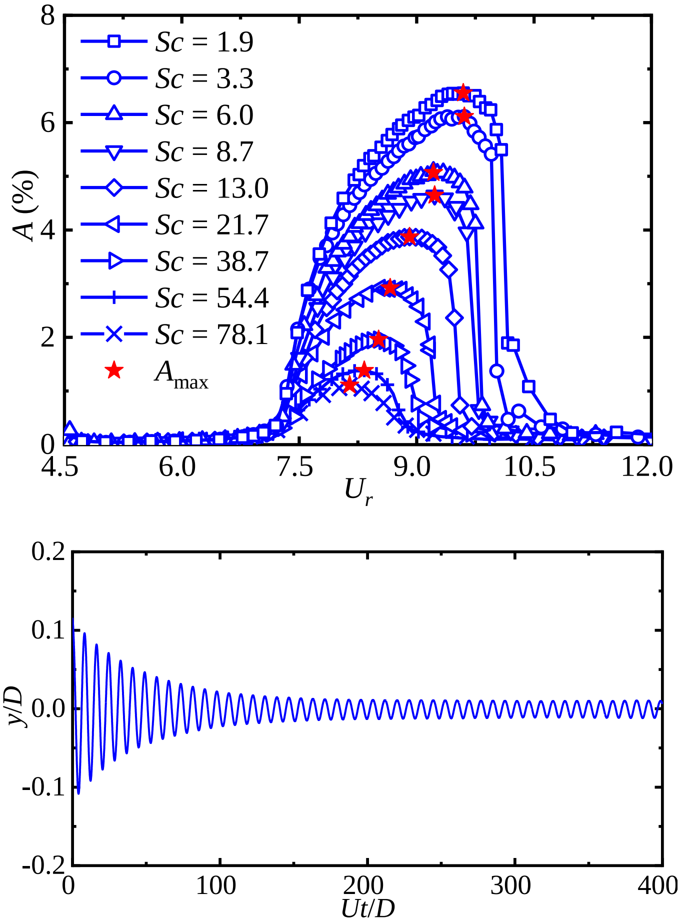

(a)

(b)

Fig. 3. VIV responses of a B/D = 4 rectangular cylinder: (a) dimensionless VIV amplitudes A at various mass-damping conditions Sc; (b) dimensionless displacement time history y/D at reduced wind speed U_r = 8.14 and Sc = 78.1. The peak VIV amplitudes A_{max} at various Sc are highlighted by red star markers.

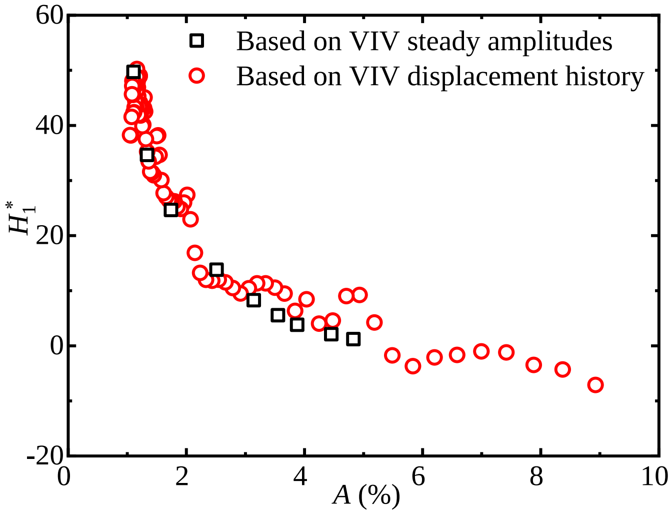

Fig. 4. Aerodynamic describing functions H_1^* of a B/D = 4 rectangular cylinder for U_r = 8.14 identified based on VIV steady amplitudes at various mass-damping conditions, and based on displacement history at a single mass-damping condition, Sc = 78.1.

537 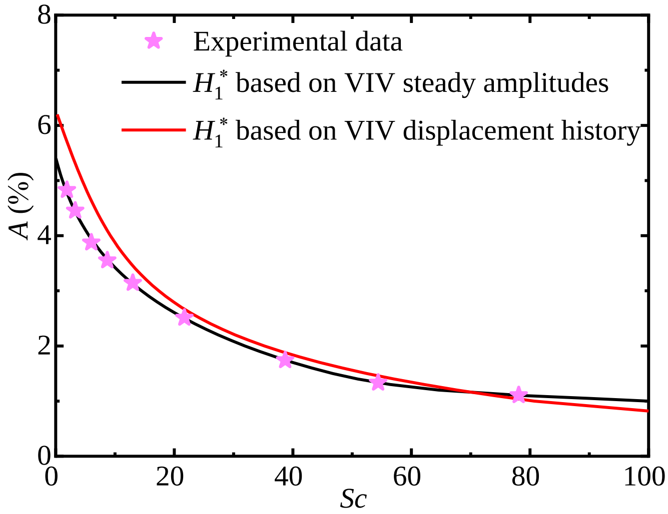

538 **Fig. 5.** Comparison between experimental and predicted VIV amplitudes A of a B/D = 4 rectangular

539 cylinder at various mass-damping conditions Sc for reduced wind speed U_r = 8.14.

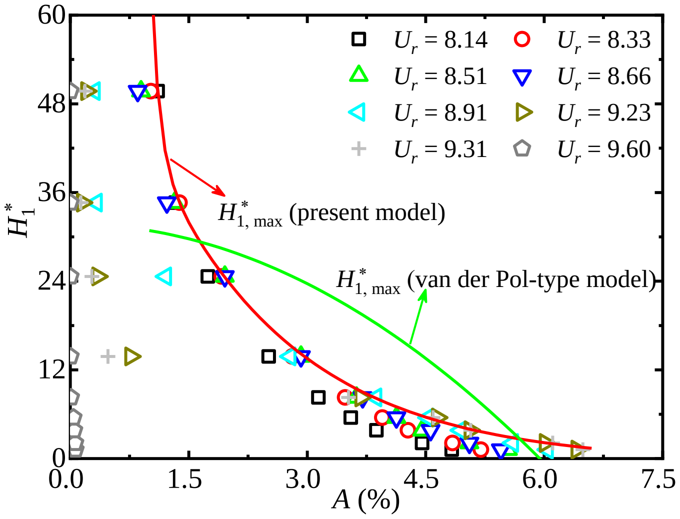

Fig. 6. Aerodynamic describing functions H_1^* and aerodynamic envelope $H^*_{1,\ \mathrm{max}}$ (red line) of a B/D = 4 rectangular cylinder. H_1^* for various U_r are identified based on the VIV steady amplitudes in Fig. 3(a). $H^*_{1,\ \mathrm{max}}$ are fitted using Eq. (12) according to the present model, and using a polynomial with linear and third order nonlinear terms according to the van der Pol-type model.

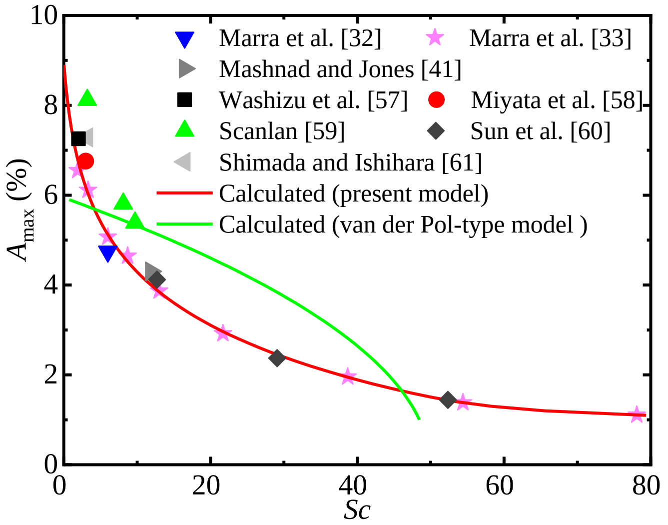

Fig. 7. Comparison between experimental and predicted peak VIV amplitudes A_{max} of a B/D = 4 rectangular cylinder at various mass-damping conditions Sc. Experimental data are obtained by various authors with different modal parameters. A_{max} are predicted by the present model and van der-Pol type model.

550
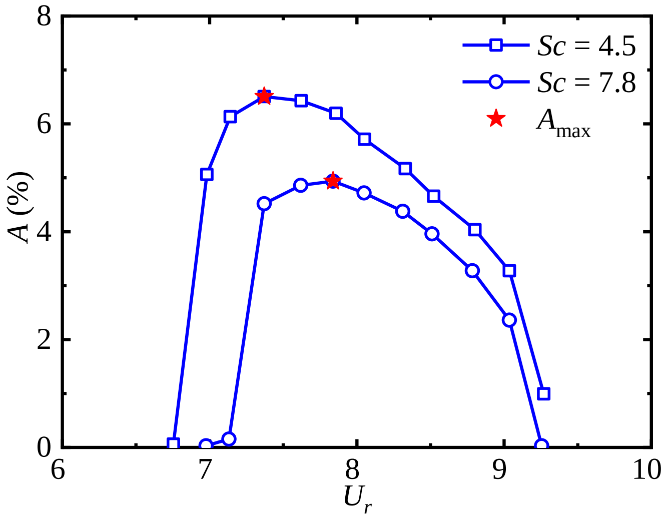

551 **Fig. 8.** Dimensionless VIV amplitudes A of a centrally slotted box deck at two mass-damping
552 conditions Sc. The peak VIV amplitudes A_{max} are highlighted by red star markers.

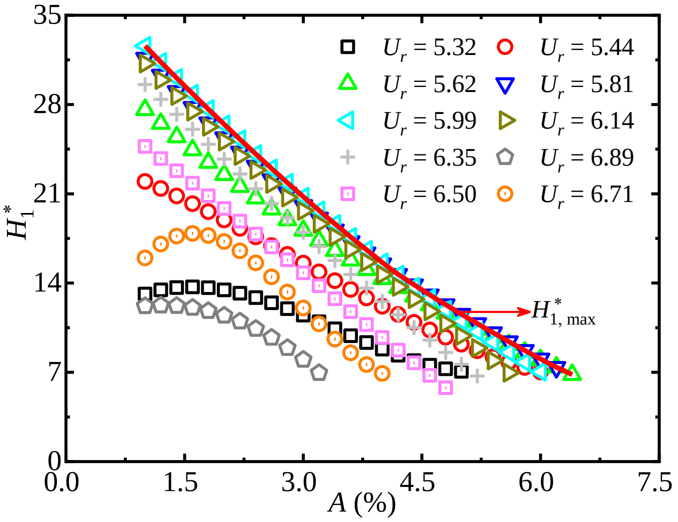

Fig. 9. Aerodynamic describing functions H_1^* and aerodynamic envelope $H_{1,\ \mathrm{max}}^*$ (red line) of a centrally slotted box deck. H_1^* for various U_r are identified based on the displacement signals at the lower tested mass-damping condition, Sc = 4.5. $H_{1,\ \mathrm{max}}^*$ is fitted using Eq. (12) according to the present model.

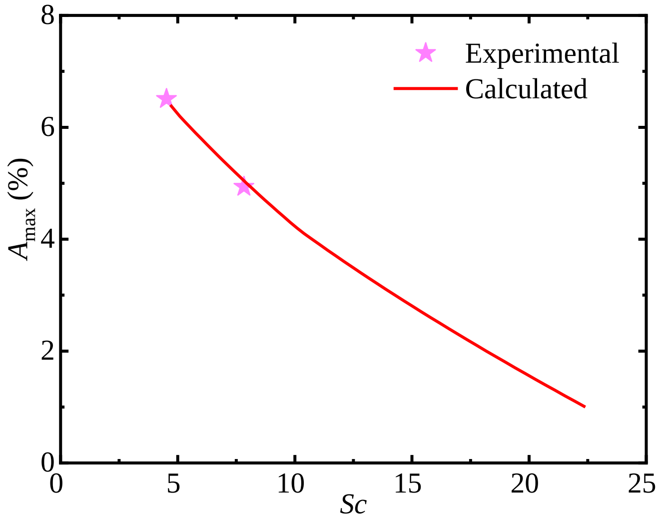

Fig. 10. Comparison between experimental and predicted peak VIV amplitudes A_{max} of a centrally slotted box deck at various mass-damping conditions *Sc*. A_{max} are predicted by the present model using the aerodynamic envelope $H^*_{1,\ max}$ presented in Fig. 9.

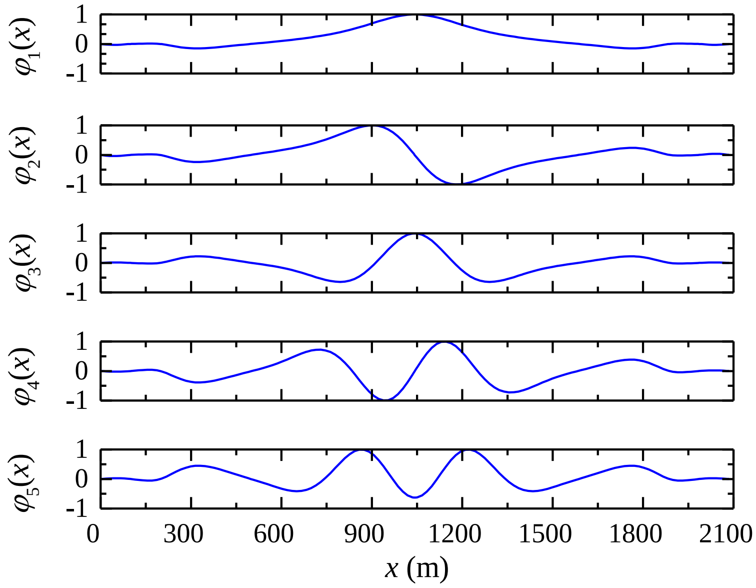

Fig. 11. Vertical mode shapes of a cable-stayed bridge deck with span arrangement of 100 × 2 + 300 + 1088 + 300 + 100 × 2 m.

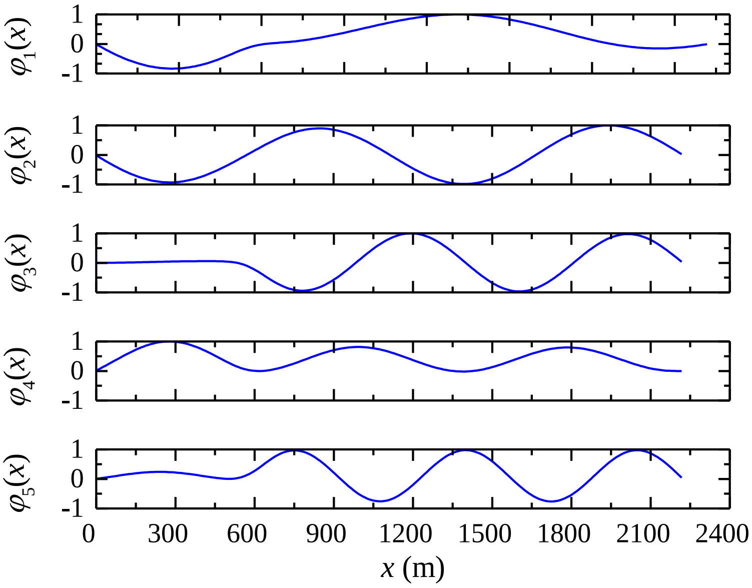

Fig. 12. Vertical mode shapes of a suspension bridge deck with span arrangement of 576 + 1650 m.

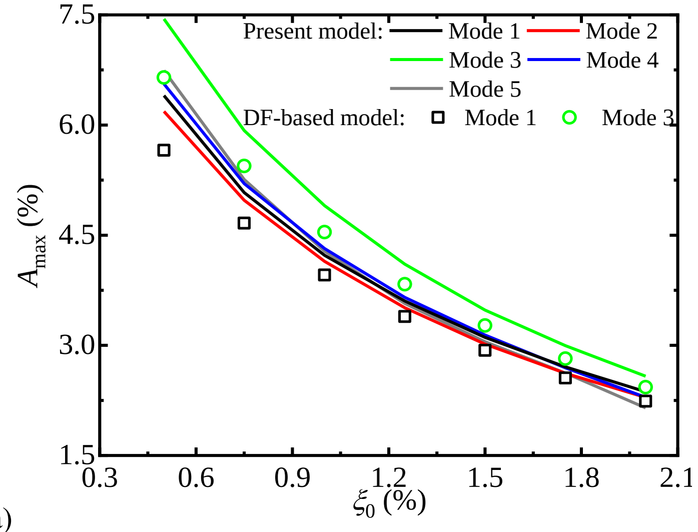

(a)

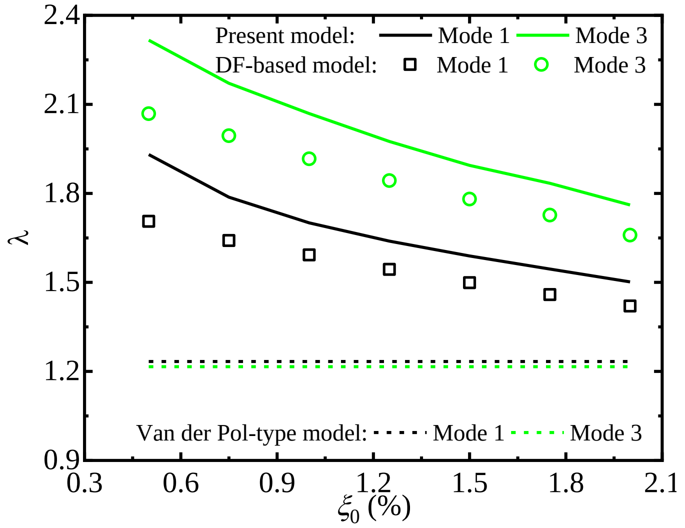

(b)

Fig. 13. Peak VIV amplitudes A_{max} and mode shape correction factors λ (i.e., ratio between the A_{max} of a flexible bridge deck to that of its rigid counterpart) of a cable-stayed bridge deck at various mechanical damping levels ξ_0: (a) A_{max} at various ξ_0; (b) λ at various ξ_0. DF: describing function.

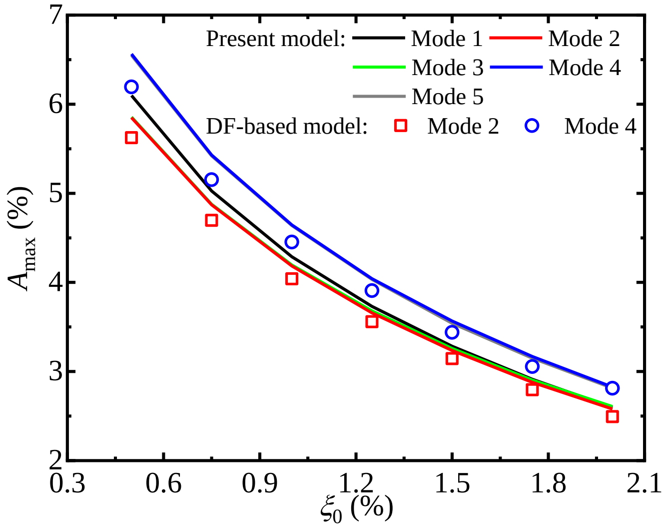

(a)

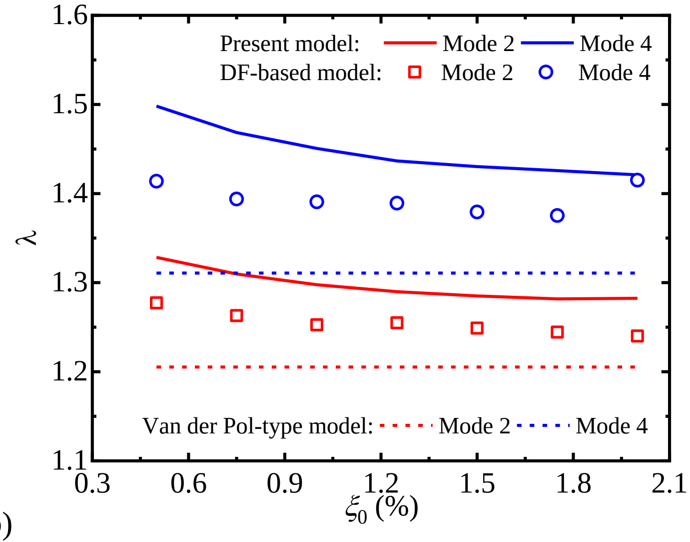

(b)

Fig. 14. Peak VIV amplitudes A_{max} and mode shape correction factors λ (i.e., ratio between the A_{max} of a flexible bridge deck to that of its rigid counterpart) of a suspension bridge deck at various mechanical damping levels ξ_0: (a) A_{max} at various ξ_0; (b) λ at various ξ_0. DF: describing function.

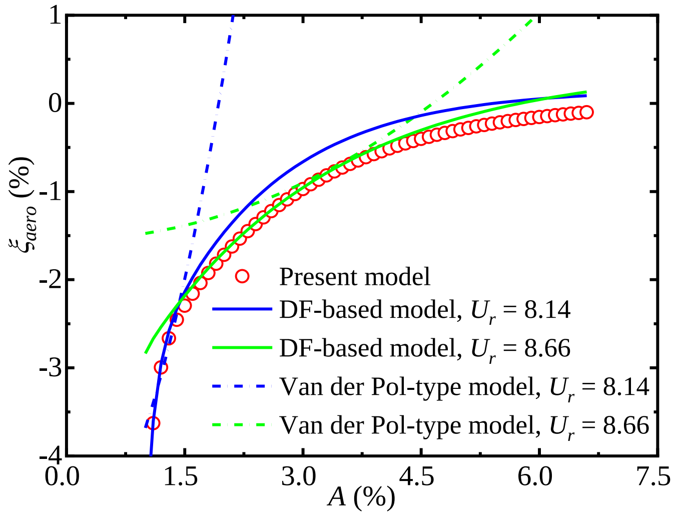

Fig. 15. Equivalent aerodynamic damping ratios ξ_{aero} of present model, describing function (DF)-based model, and van der Pol-type model. A is the dimensionless vibration amplitude. Results of the present model is constructed from the aerodynamic envelope, while results for the DF-based model and van der Pol-type model are constructed from the aerodynamic parameters at two different reduced wind speeds, U_r = 8.14 and 8.66.